P. Schuepbach[1]
e-mail: schuepbach@lec.mavt.ethz.ch

R. S. Abhari

Department of Mechanical and Process Engineering,
LEC,
Laboratory of Energy Conversion,
ETH Zurich,
Zurich CH-8092, Switzerland

M. G. Rose
Institute of Aeronautical Propulsion,
University of Stuttgart,
70569 Stuttgart, Germany

T. Germain

I. Raab

J. Gier

MTU Aero Engines GmbH,
Dachauer Strasse 665,
80995 München, Germany

Effects of Suction and Injection Purge-Flow on the Secondary Flow Structures of a High-Work Turbine

In high-pressure turbines, a small amount of air is ejected at the hub rim seal to cool and prevent the ingestion of hot gases into the cavity between the stator and the disk. This paper presents an experimental study of the flow mechanisms that are associated with injection through the hub rim seal at the rotor inlet. Two different injection rates are investigated: nominal sucking of −0.14% of the main massflow and nominal blowing of 0.9%. This investigation is executed on a one-and-1/2-stage axial turbine. The results shown here come from unsteady and steady measurements, which have been acquired upstream and downstream of the rotor. The paper gives a detailed analysis of the changing secondary flow field, as well as unsteady interactions associated with the injection. The injection of fluid causes a very different and generally more unsteady flow field at the rotor exit near the hub. The injection causes the turbine efficiency to deteriorate by about 0.6%. [DOI: 10.1115/1.4000485]

1 Introduction

In order to improve the thermal cycle efficiency of gas turbines, turbine entry temperatures have been continuously increased over the past decades. With these increases the ingestion of hot gases into the disk cavities has become an issue, as it can cause overheating of the disks, as well as thermal fatigue of the components. In order to mitigate the adverse effects of ingestion of hot gases, bypassed compressor air is injected through the rim seals between the rotating and stationary parts. The goal is to minimize the amount of injection massflow and to reduce the aerodynamic losses, which can be attributed to the injection. The ingestion of hot gases is driven by both disk pumping, as well as the external nonaxisymmetric pressure field. This has been experimentally investigated in previous studies; Kobashi et al. [1] found that the pressure difference criterion underestimates the minimum cooling flow rate. Chew et al. [2] and Dadkhah et al. [3] also examined the question of the minimum coolant flow that is required to prevent ingestion and where the ingested air would end up in the cavity. The pressure field is however highly unsteady due to stator-rotor interactions. Roy et al. [4], for example, showed that the effect of the unsteady pressure field was much more pronounced inside the cavity than the time-averaged circumferential external pressure field. Recent research has focused on the flow interactions between the cooling air and the mainstream flow. McLean et al. [5,6] tested radial, impingement, and root injection cooling configurations. They observed that root injection had the most pronounced effect on the loss coefficient and total-to-total efficiency. Furthermore they found profound effects on the secondary flows of the following row. Girgis et al. [7] compared radial injection to compound injection, which had both radial and tangential components. They observed that the latter resulted in an efficiency improvement. Ong et al. [8] also concluded that some of the efficiency penalty due to coolant could be regained by introducing a swirl component to the coolant jet. Furthermore they found that most of the coolant is entrained by the downstream blade hub secondary flow. Paniagua et al. [9] reported that there is an intensification of the rotor hub vortex and an enhancement of the radial migration due to injection. In recent studies the importance of the unsteady interaction of the freestream and the cavity were highlighted. Boudet et al. [10] found frequencies that are unrelated to the blade passing frequency. They attributed this to a nonlinear coupling of the blade passing frequency with an instability formed inside the cavity. They concluded that only full annulus and unsteady modeling would capture the experimentally observed flow phenomena. Reid et al. [11] quantified the efficiency penalty caused by the rim seal flow to be about 0.56% for 1.0% of injection massflow. Marini and Girgis [12] in a numerical study examined the effects of the blade leading edge platform and noted that there is a 0.07% stage efficiency benefit and a reduced sensitivity to an increasing cavity massflow.

The present work shows performance sensitivities for purge flow. Intensification of the secondary flows at exit of the rotor and a higher penetration of the secondary flows with purge flow are observed. A detailed time-resolved measurement and analysis with and without purge flow are presented. By a spectral analysis at exit of the rotor with purge, flow subharmonic frequencies are resolved.

2 Experimental Method

2.1 Experimental Turbine Facility. The experimental investigation was performed in the research turbine "LISA" in the Laboratory of Energy Conversion at Swiss Federal Institute of Technology. Recently the existing two-stage, shrouded turbine configuration [13] was redesigned as a one-and-1/2 unshrouded

[1]Corresponding author.

Contributed by the International Gas Turbine Institute (IGTI) of ASME for publication in the JOURNAL OF TURBOMACHINERY. Manuscript received August 20, 2008; final manuscript received August 29, 2008; published online January 21, 2010. Editor: David Wisler.

Table 1 Characteristic geometry

	Stator 1	Rotor
No. of blades	36	54
Inlet angle (midspan) (deg)	0	54
Exit angle (midspan) (deg)	73	−67
Solidity (chord/pitch)	0.87	1.17
Aspect ratio (span/chord)	1.27	1.41
Profile stacking	LE	CoG

turbine that is representative of a high work cooled turbine. Further details of the new design are presented by Behr et al. [14], but its salient features are described below.

The air-loop of the facility is a quasiclosed type and includes a radial compressor, a two-stage water to air heat exchanger and a calibrated venturi nozzle for mass flow measurements. Upstream of the turbine section is a 3 m part with flow straighteners to ensure a homogenous flow field. Additionally the flow undergoes an acceleration ahead of the turbine section in order to reduce the significance of any remaining flow nonuniformities. At the exit of the turbine section the air-loop opens to atmosphere. A dc generator absorbs the turbine power and controls the rotational speed with an indicated accuracy $\pm 0.02\%$ ($\pm 0.5RMP$). A heat exchanger controls the $T_{t,\mathrm{in}}$ to an accuracy of $\pm 0.3\%$. A torquemeter measures the torque on the rotor shaft. With a compressor ratio limited to $\Pi_{c,\max}=1.5$, it is necessary to add a tandem deswirl vane arrangement to recover the static pressure at the exit of the second stator back to the ambient level, in order to reach the intended turbine pressure ratio of $\Pi_{1.5}=1.65$. The turbine is unshrouded with a nominal tip gap of 1% of the span. The variation in the tip gap between builds is less than 1% of the tip gap, which ensures a good repeatability.

Table 1 gives the general geometrical data of the first stage of the investigated turbine. A new air-system was designed to provide the possibility of injection of air through the rotor upstream rim seal. The air is bled off the primary air-loop upstream of the flow conditioning stretch. The bleed air passes through a venturi to measure the bypassed massflow. Finally the bypass flow enters a plenum from where ten plastic pipes lead the flow to ten first nozzle guide vane rows (NGV1s). Through these NGV1s the flow enters the cavity labeled **B** in Fig. 1. From the cavity underneath the NGV1s there are two leakage paths indicated in Fig. 1 as dotted arrows **P** and **S**. One path is through the upstream rim seal into the mainflow **P**. The rest of the gas is ejected through the drum to the ambient after being measured in another venturi called the secondary massflow **S**. The pressure difference over the labyrinth seal leading from the downstream rim seal into the drum is balanced. Under these conditions the net massflow through the downstream rim seal into the drum is assumed to be zero. Thus the injection or purge massflow can be calculated as the difference of the bypass massflow and secondary massflow. Previously it was only possible to run the rig with the upstream rim seal in a sucking mode.

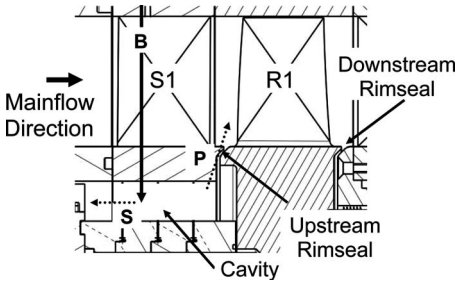

Fig. 1 Illustration of leakage path

Table 2 Operating conditions

$\Pi_{1.5}$	$1.65 \pm 0.4\%$
$T_{t,\mathrm{in}}$	328 ± 0.2 K
$\frac{\dot{m}\sqrt{T_{t,\mathrm{in}}}}{p_{t,\mathrm{in}}}$	$152 \pm 0.2\%$ $\left(\frac{\mathrm{kg\ K^{1/2}}}{\mathrm{s\ bar}}\right)$
$\frac{N}{\sqrt{T_{t,\mathrm{in}}}}$	2.48 ± 0.05 $\frac{\mathrm{rps}}{\mathrm{K^{1/2}}}$

2.2 Measurement Technology. The steady flow field is measured with a miniature cobra-head five-hole probe with a tip diameter of 0.9 mm. The unsteady flow field is measured with a fast response aerodynamic probe (FRAP), which was developed at the LEC [15,16]. The probe is capable of capturing unsteady flow features of up to frequencies of 48 kHz based on measurements including total and static pressures, flow yaw and pitch angles, and Mach number. The frequency bandwidth of the temperature is limited to a frequency of 10 Hz. However the influence of the temperature on the velocity is very modest. The used FRAP probe has a 1.8 mm tip diameter and is equipped with two sensors. The probe is operated in a virtual-four-sensor mode to measure three-dimensional time-resolved flow properties. The measurement grid consisted of 39 radial and 40 circumferential points (covering one stator pitch) with a radial clustering near the endwalls. The data are acquired at a sampling rate of 200 kHz over a period of 2 s. During the data processing a phase lock averaging over 85 rotor revolutions per rotor pitch is used. The postprocessing is done for three consecutive rotor pitches. The sampling rate resolves 82 points per rotor pitch in the relative frame of reference.

3 Results and Discussion

3.1 Operating Conditions. During measurements the turbine 1(1/2) stage total-to-static pressure ratio is kept constant at $\Pi_{1.5}=1.65$. The entry temperature is kept constant to permit an accurate comparison between measurements made on different days. To account for the change in ambient pressure on different measurement days the pressures are nondimensionalized by the respective inlet total pressure. The operating conditions are given in Table 2.

In this paper the data of two different injection rates are compared. The definition of the injection rate is given in Eq. (1).

$$IR = \frac{\dot{m}_{\mathrm{by}} - \dot{m}_{\mathrm{dr}}}{\dot{m}_v} \cdot 100 \tag{1}$$

The tests were conducted with two different IRs -0.14% and 0.9%. At -0.14% the rim seal is nominally in a modest sucking mode, while at 0.9% it is said to be blowing.

3.2 Performance Sensitivity. In this section the sensitivity of the total-to-total efficiency to different injection rates is presented. The definition of efficiency used in this study, accounting for the injection is given in Eq. (2)

$$\eta_{tt} = \frac{\dfrac{\omega \cdot M}{\dot{m}_v \cdot c_p \cdot T_{t,\mathrm{in}}}}{1 - \left(1 - \dfrac{IR}{100}\right) \cdot \left(\dfrac{p_{t,R1\mathrm{ex}}}{p_{t,\mathrm{in}}}\right)^{\gamma-1/\gamma} - \dfrac{IR}{100} \cdot \left(\dfrac{p_{t,R1\mathrm{ex}}}{p_{t,\mathrm{cav}}}\right)^{(\gamma-1)/\gamma}} \tag{2}$$

The efficiency drop is $\Delta\eta_{tt}=0.6\%$ when comparing the sucking case ($IR=-0.14\%$) to the blowing case ($IR=0.9\%$).

Figure 2 shows the circumferentially massflow averaged relative flow yaw angle at the exit of the rotor. The design metal angle is −67 deg over the whole span. At the hub one can see the underturning region between 20% and 30% span.

At 10% span there is the overturning region induced by the hub passage vortex. At 72% span the tip passage vortex introduces

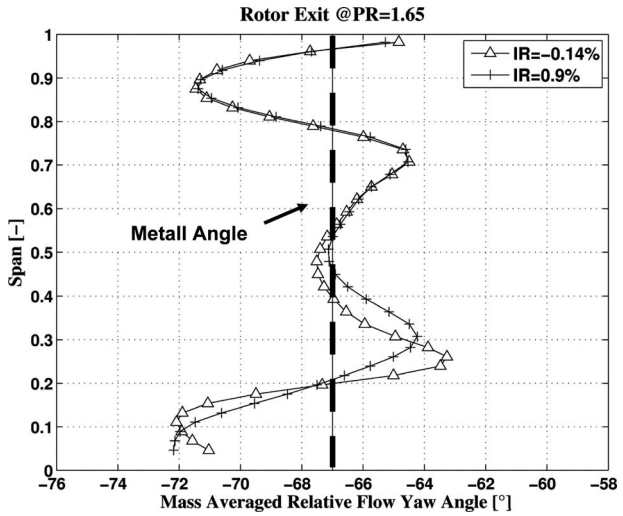

Fig. 2 Mass-averaged relative flow angle traverse plane *R*1ex

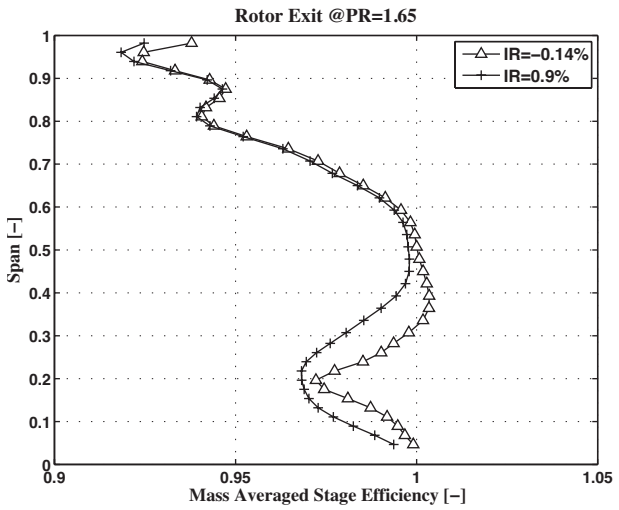

Fig. 3 Mass-averaged total-to-total efficiency traverse plane *R*1ex

underturning. At 88% span there is the combined overturning of the tip passage vortex and the tip leakage vortex. Finally at the casing the underturning part of the tip leakage vortex can be seen. In the outer half of the annulus there is no influence of the injection. At the hub the underturning is reduced by 1.4 deg with purge flow, while it radially migrated outwards by 5% of the span. The overturning is the same in both cases. With purge flow the highest overturning is at a 5% lower span position. With purge flow the signature of the secondary flow is diminished, while it has a larger radial extent.

Figure 3 shows the radial distribution of the total-to-total efficiency. It should be noted that this efficiency is linearly related to the total pressure distribution since the power used to calculate it is only a one-dimensional (1D) value. The efficiency is nondimensionalized with the midheight value of the ($IR=-0.14\%$) sucking case. There is an increasing efficiency deficit toward the hub for the injection case. The suction case has a more pronounced loss core around 20% span, while it is more diffused in the purge flow case.

3.3 Time-Resolved Data. Figure 4 shows the relative total pressure field of the blowing case with an injection rate of 0.9% for two stator pitches at exit of the rotor. As the vane to blade ratio is two to three, the loss systems of three rotor blades can be seen. Figure 4 shows the situation at one instant in time in the absolute frame. The rotor loss features can be identified as the low relative total pressure zones.

From 90% span up to the casing the loss is associated with the tip leakage vortex labeled with 1. Between 65% and 80% span the tip passage vortex loss 2. In between 30% and 65% span the rotor wake can be identified. From 10% to 30% span the low relative total pressure zone shows the rotor hub passage vortex 3. The low momentum purge flow is entrained by the hub passage vortex of the rotor. This results in a large and diffused region at the hub.

Based on the stationary flow field three different interaction zones in the rotor exit flow field can be identified. The centerlines of these regions are seen as radial lines in Fig. 4 labeled with **A**, **B**, and **C**. In the region along traverse **A** the loss features of the upstream nozzle appear. Sharma et al. [17] called this region *minimum interaction time location* as the nozzle flow features pass through the rotor passage with minimal interaction with the rotor leading edge. Traverse **B** is in the middle of a high relative total pressure zone caused by the pressure waves of the downstream nozzle. In the region around traverse **C** there is no interaction of the rotor flow features with either the upstream nozzle or the downstream nozzle. Sharma et al. [17] showed that this region is

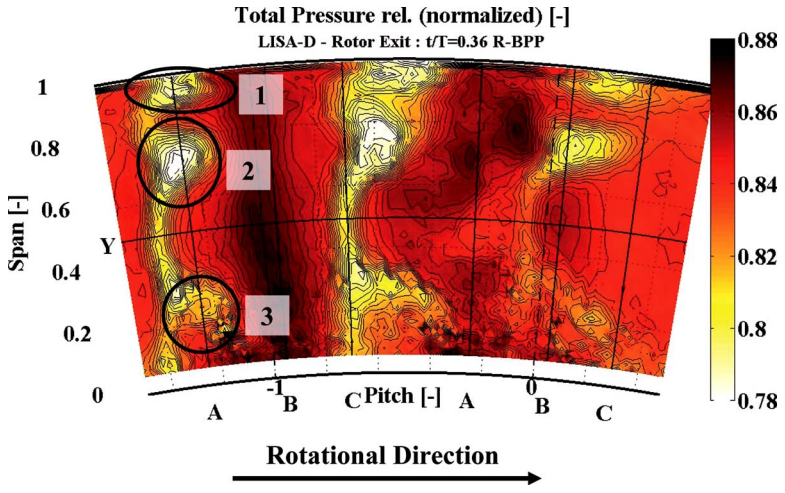

Fig. 4 Relative total pressure for blowing *IR*=0.9% at traverse plane *R*1ex

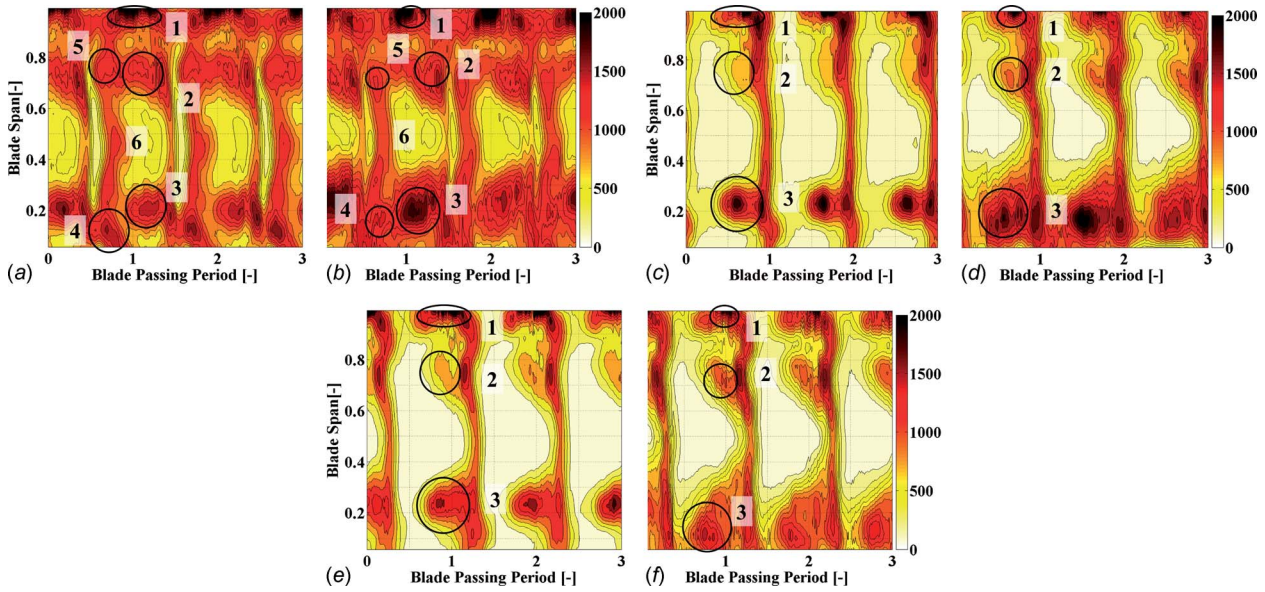

Fig. 5 rms of random part of total pressure at traverse plane *R*1ex (Pa)

characterized by low turbulence values and that the flow field is quite similar to the one, which would be observed in cascade tests. To better understand the different interactions in region **A**, **B**, and **C**, these traverses are plotted against time, as seen in Figs. 5–7.

Figure 5 shows the rms values of the random part of the total pressure signal as a plot of radius against time for the three traverses. Using the triple decomposition of the time-resolved pressure signal as shown in Eq. (3) the random part $p'(t)$ can be evaluated as the difference between the time-resolved pressure $p(t)$ and the phase-locked averaged pressure $\bar{p}+\tilde{p}(t)$. The same

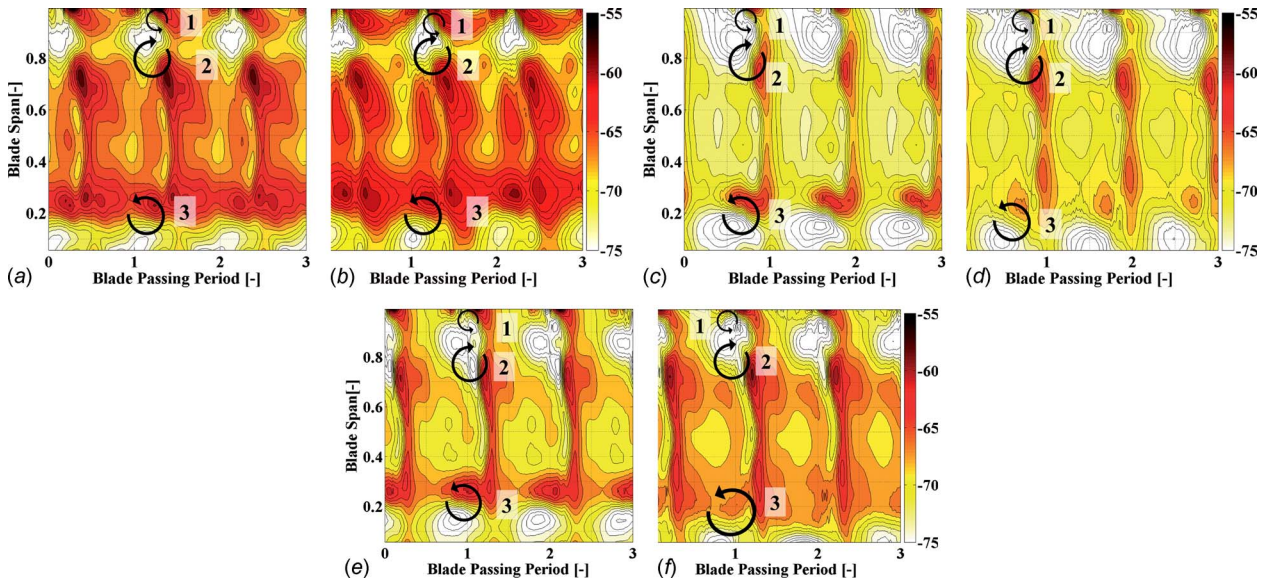

Fig. 6 Relative flow angle traverse plane *R*1ex

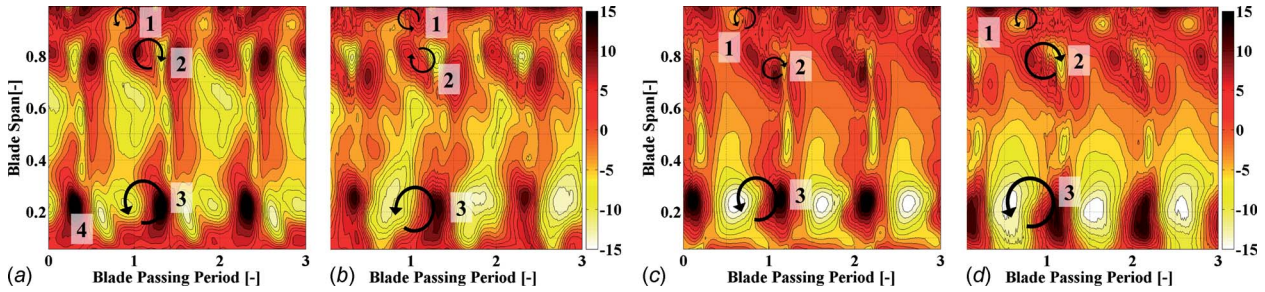

Fig. 7 Pitch angle at traverse plane *R*1ex

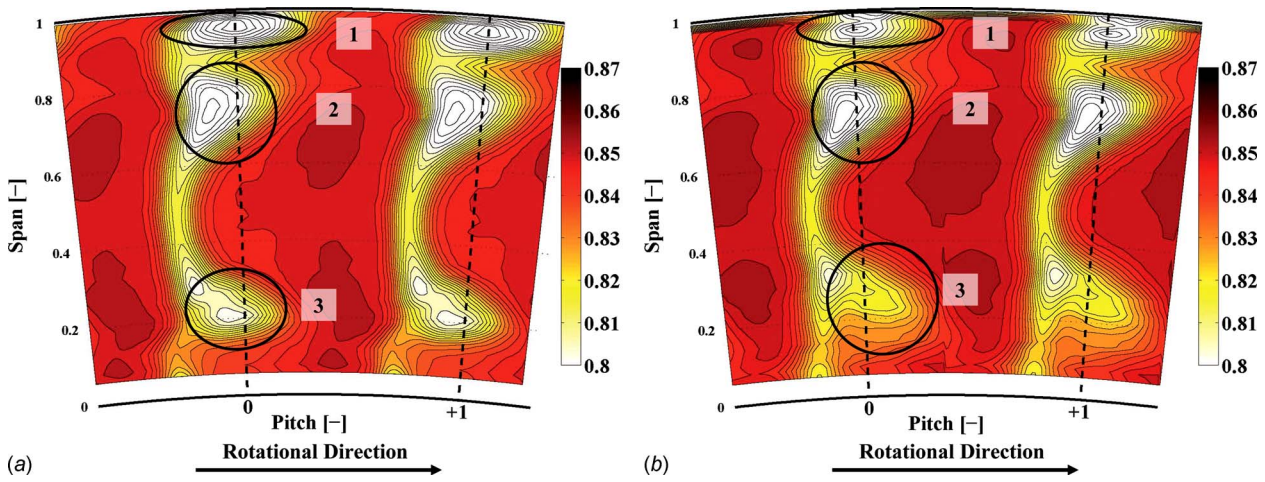

Fig. 8 Time-averaged relative total pressure in the rotor frame of reference at traverse plane *R*1ex

approach was used by Porreca et al. [18] to derive turbulent quantities.

$$p(t) = \bar{p} + \tilde{p}(t) + p'(t) \tag{3}$$

Figures 5(*e*) and 5(*f*) show only minor rotor-stator interactions characterized by the lowest integral rms values. The rotor flow features identified in Fig. 4 can be seen as high rms regions. From 90% span to the tip one can identify the tip leakage vortex labeled with 1 in between 60% and 80% span the rotor tip passage vortex 2, and finally between 15% and 35% span the rotor hub passage vortex 3. With purge flow the highest unsteadiness in the hub passage vortex is constrained to the hub and diffused over a larger area.

In traverse **B** the unsteadiness in the rotor hub passage vortex rises due to the interaction with the downstream stator leading edge. The purge flow case shows a much stronger increase in rms. This could be the signature of a vortex break down.

Along traverse **A** the integral rms values rise once more as additional high rms zones are occurring. These zones show the remains of the upstream vane flow features. There is a high rms zone at the hub labeled 4 associated with the upstream vane hub passage vortex. With purge flow the high rms zone of the rotor hub passage vortex 3 is lifted of the endwall once it starts to interact with the upstream vane hub passage vortex 4. This is probably happening as the leakage fluid has very little momentum.

If streamwise vorticity is present in a flowfield one will find radial gradients of yaw angle, as well as circumferential gradients of pitch angle. As the rotor vorticities travel through the radial traverse, the time gradients are related to the circumferential gradients in the rotating frame. Therefore the strength of the radial yaw angle and the time gradient of the pitch angle are good indicators of the strength of the streamwise vorticity.

Figure 6 shows the relative flow angle in the time-space format. At the hub there is a positive radial gradient of the relative flow angle associated with the hub passage vortex 3. In traverse **B** and **C** this gradient is lowered by a factor of about 5–6 with purge flow present. In traverse **B** it has been reduced from 4.9 deg/mm to 1.0 deg/mm with purge flow and at traverse **C** from 4.6 deg/mm to 0.8 deg/mm. At traverse **A** the gradients are about the same size 1.4 deg/mm and 1.6 deg/mm for both injection cases. This leads to the conclusion that the hub passage vortex of the purge flow case shows a different behavior once the vortex starts to interact with the upstream vane features as seen in traverse **A**. With purge flow the vortex is gaining intensity as it starts to interact with the upstream flow features. Without purge flow the vortex loses intensity.

Figure 7 shows the radial-time diagram for the pitch angle of traverse **A** and **C**. Traverse **C** shows pitch angle variations caused by the rotor flow features. Between 10% and 30% span there is a positive temporal pitch angle gradient, which is the signature of the rotor passage vortex 3. The maximum pitch angle gradient is at 27% in the sucking case and at 21% in the blowing case. The gradient reduced by 2.7 deg per blade passing period with purge flow. This indicates a lower vorticity peak closer to the hub. In traverse **A** the maximum temporal pitch angle gradient can be found at 23% in the sucking case and at 26% in the blowing case. With purge flow the positive gradient at the hub is reduced by 3.5 deg per blade passing period in this circumferential location. With purge flow the rotor hub passage vortex migrates outwards going from traverse **C** to **A**. This reconfirms the observation made further up that the hub passage vortex lifts of the endwall once it starts to interact with the upstream vane flow features, as seen in traverse **A** if purge flow is present.

3.4 Rotating Frame Time-Averaged Results. Figure 8 shows the relative total pressure at the rotor exit time-averaged in the rotating frame of reference. Below 30% span there is the low relative total pressure zone that is associated with the rotor hub passage vortex 3. Between 65% and 80% the tip passage vortex loss core can be identified as 2. Between 90% span and the casing there is the signature of the tip leakage vortex 1. The narrow band of low relative total pressure between 30% and 65% represents the rotor wake. In the purge flow case the hub loss zone is about twice the size of the zone in the sucking case. This loss zone extends from 40% span down to the measurement line closest to the hub

$$Y_{\text{rel}}(r) = \frac{p_{\text{trel,S1ex}}(r) - p_{\text{trel,R1ex}}(r)}{p_{\text{trel,R1ex}}(r) - p_{s,R1\text{ex}}(r)} \cdot 100 \tag{4}$$

Equation (4) gives the definition for the relative total pressure loss coefficient Y_{rel}. Figure 9 shows the radial distribution of Y_{rel} determined with the mass-averaged relative total pressure values at the same radial height. Figure 9 confirms the observations made in Fig. 8. The peak loss in both cases is the same within 1%. The purge flow however shows loss over a much larger radial extent, resulting in an 18% higher integral hub loss.

Figure 10 shows the streamwise vorticity at the rotor exit time-averaged in the rotating frame of reference. The positive streamwise vorticity seen at 20% span and labeled 3 is due to the rotor hub passage vortex. The negative vorticity region 5 can be associated with the trailing edge shed vortex. At 75% the vorticity of the tip passage vortex can be seen in region 2. The tip shed vortex is labeled 4. Along the casing the positive vorticity signature of the tip leakage vortex is seen in region 1. With purge flow the peak vorticity of the hub passage vortex is about halved. This agrees with the observation made in the radial-time plots of the pitch and relative flow angle, as seen Figs. 6 and 7. However the

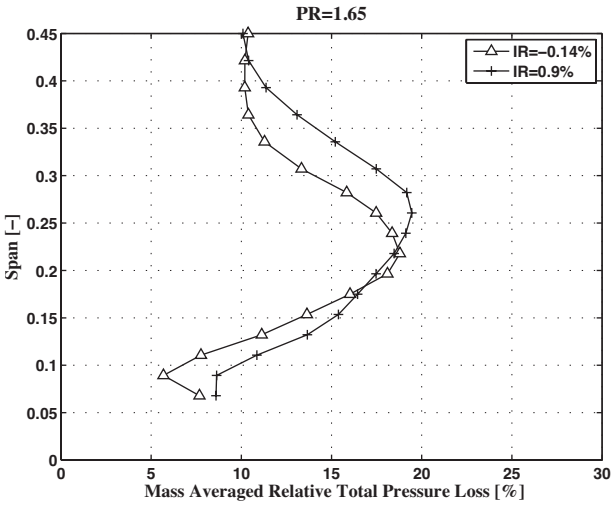

Fig. 9 Time-averaged and circumferentially mass-averaged in the rotor frame of reference relative total pressure loss at traverse plane *R*1ex (%)

integrated circulation is 10% higher with injection. The integrated circulation of the hub trailing shed vortex has increased by 30%. This indicates a greater variation in blade lift with span. Therefore the lift at the hub must have reduced. The purge flow shows no significant influence in the outer annulus half.

Figure 11 shows the time-averaged rms values of the random part of the total pressure signal in the rotating frame of reference. There are three distinct regions of high rms values representing the hub passage vortex (below 40% Span) 3, the tip passage vortex (between 60% and 80% Span) 2 and the leakage vortex (beyond 90% span) 1. Furthermore there is a band of high rms values between 40% and 60% span associated with the rotor wake. The rms plot shows a very diffused hub passage vortex region with purge flow, which has increased in size and reduced in peak intensity compared with the sucking case.

The rate of irreversible heat generation by doing work against the viscous forces is given in Eq. (5) given in Ref. [19]. The parameter Φ is the dissipation function. The viscosity in Eq. (5) is the molecular or laminar viscosity. In order to evaluate the dissipation correctly one would need a very fine spatial resolution. The instantaneous velocity vector with its deterministic and turbulent fluctuations is also needed. In practice the spatial resolution is limited by the traverse grid size and the temporal resolution is only deterministic. For these reasons the calculated dissipation must be regarded with some care as the modest spatial resolution and the deterministic time signature will result in an underestimate of the dissipation

$$dQ_F = dt \cdot \Delta V \cdot \mu \cdot \Phi \tag{5}$$

Φ, the viscous dissipation function, is given in cylindrical coordinates in Eq. (6). The required axial gradients are approximated using a frozen flow structure assumption. The detailed approach can be found in Ref. [20]

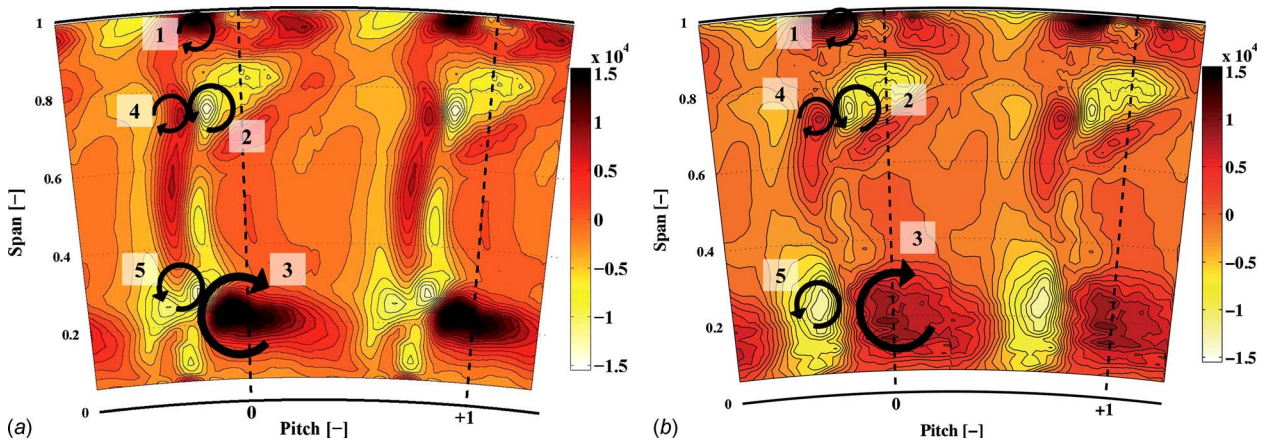

Fig. 10 Time-averaged streamwise vorticity in the rotor frame of reference at traverse plane *R*1ex (1/s)

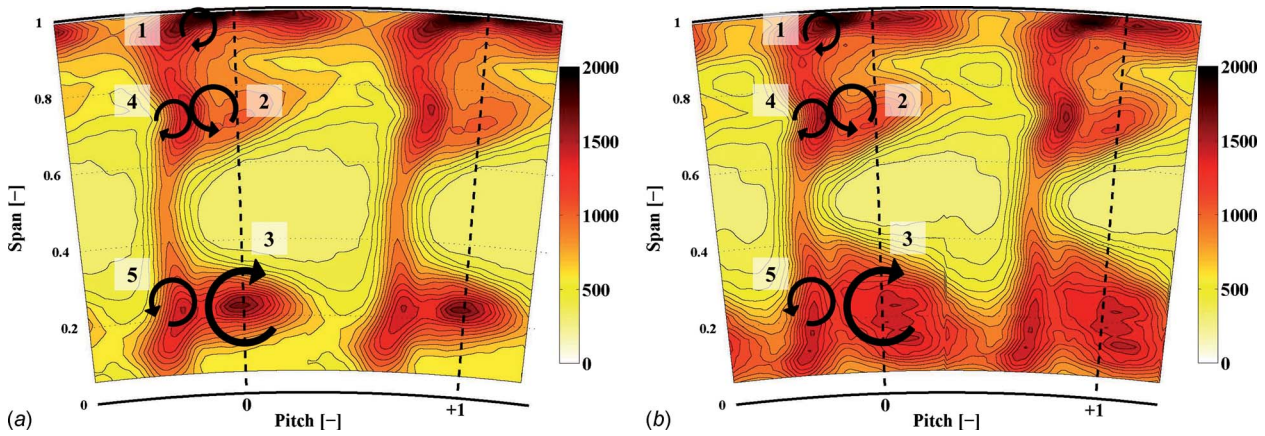

Fig. 11 Time-averaged rms of random part of total pressure in the rotor frame of reference at traverse plane *R*1ex (Pa)

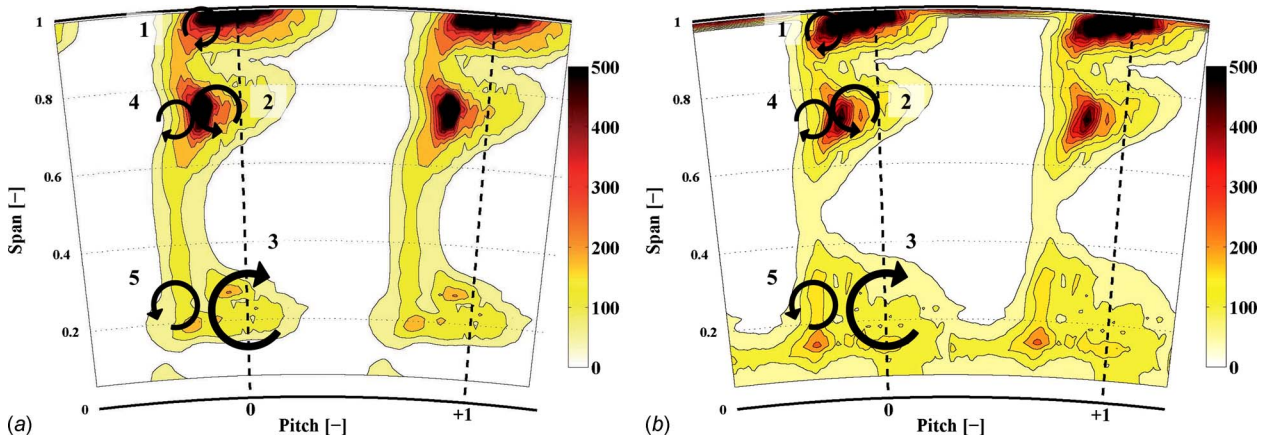

Fig. 12 Time-averaged *D* parameter in the rotor frame of reference at traverse plane *R*1ex (%/s)

$$\Phi = 2\left[\left(\frac{\partial u_r}{\partial r}\right)^2 + \left(\frac{1}{r}\frac{\partial u_\theta}{\partial \theta} + \frac{u_r}{r}\right)^2 + \left(\frac{\partial u_x}{\partial x}\right)^2\right] + \left[r\frac{\partial}{\partial r}\left(\frac{u_\theta}{r}\right) + \frac{1}{r}\frac{\partial u_r}{\partial \theta}\right]^2 + \left[\frac{1}{r}\frac{\partial u_x}{\partial \theta} + \frac{\partial u_\theta}{\partial x}\right]^2 + \left[\frac{\partial u_r}{\partial x} + \frac{\partial u_x}{\partial r}\right]^2 - \frac{2}{3}(\nabla \cdot \underline{u})^2 \tag{6}$$

In order to better quantify the dissipation function, it is normalized by the flux of kinetic energy given in Eq. (7)

$$\dot{m} \cdot \frac{u^2}{2} = \rho \cdot u_x \cdot A_x \cdot \frac{u^2}{2} \tag{7}$$

where

$$u^2 = u_x^2 + u_r^2 + u_\theta^2 \tag{8}$$

Thus we have the semi-nondimensional dissipation function D given in Eq. (9)

$$D = \frac{\mu \cdot \Phi}{\rho \cdot \frac{u^2}{2}} \tag{9}$$

Figure 12 shows the time-averaged D parameter at the rotor exit in the rotating frame of reference. The highest values are measured both in the tip leakage region and in the interaction zone of the tip trailing edge shed vortex 4 and the tip passage vortex 2. The dissipation at the hub is much less pronounced. The peak dissipation values are about the same in both cases. However the extension with purge flow is much larger, resulting in a 39.6 % higher integral dissipation value for the lower annulus half.

3.5 Spectral Analysis. The frequency composition of the flow in the hub loss core is determined from an fast Fourier transform (FFT) of the raw voltage signal of sensor 1 of the FRAP probe, which is directly related to the pressure signal. The amplitude is nondimensionalized by the baseline value at blade passing frequency. The measurements at 16% span and −12.5% pitch are considered. The results are presented in Fig. 13. The blade passing period is 2430 Hz. With $IR = -0.14\%$ there is a distinct peak at the blade passing frequency. With purge flow the peak amplitude at the blade passing frequency is reduced. Furthermore there is a band of relatively high amplitudes centered on the subharmonic of the blade passing frequency. The injection seems to introduce such subharmonic frequencies, as was observed by Boudet et al. [10]. They found that such frequencies result from the nonlinear interactions with cavity instabilities. In the present work no time-resolved cavity data are available. Therefore no conclusive statement on the origin of these frequencies can be made. Alternatively there are possibly some nondeterministic modes of the rotor hub secondary flows influenced by the purge flow.

4 Conclusions

The results with axisymmetric endwalls show a total-to-total efficiency drop of $\Delta\eta_{tt} = 0.6\%$ when increasing the injection from the sucking mode $IR = -0.14\%$ to the blowing mode $IR = 0.9\%$. With injection and conventional endwalls the hub secondary flows have a larger radial extent. The angles, as well as the vorticity contour plots in the rotor hub passage vortex region, show that the vorticity peak values are reduced by using purge flow. This indicates a reduced rotation of the vortex when the purge flow is entrained into the vortex. However the integrated circulation of the passage vortex with purge flow has increased by 10%. The circulation of the hub trailing shed vortex has increased by 30% with injection through the rotor upstream rim seal. The integrated dissipation function D has increased with purge flow by almost 40% explaining some of the efficiency deficit.

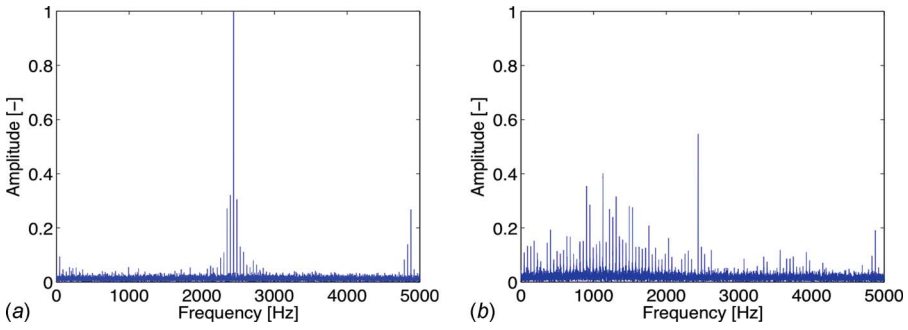

Fig. 13 FFT of the raw voltage signal of the frap probe at 16% span and –12.5% pitch

FFT results show that there is a frequency in the pressure signal of around half the blade passing frequency in the hub region, which could possibly result from a nonlinear combination with some cavity modes. Nevertheless no conclusive statement can be made as there is no time-resolved data from the cavity available.

Acknowledgment

The work leading to the results of this paper was carried out within the joint industrial and academic research program that is part of the "Luftfahrtforschungsprogramm LuFo3" supported by the German Federal Ministry of Economics and Technology.

Nomenclature

A = area (m^2)
D = semi-nondimensional dissipation function (%/s)
c_p = specific heat for constant pressure (J/kg)
IR = injection rate
M = torque (Nm)
$\dot{m}$ = massflow (kg/s)
N = rotational speed (rps)
p = pressure (Pa)
$\bar{p}$ = time mean part of pressure signal (Pa)
$\tilde{p}$ = periodic part of pressure signal (Pa)
p' = random part of pressure signal (Pa)
Q = amount of heat (J)
r = radial coordinate (m)
T = temperature (K)
T = blade period (s)
t = time (s)
u = velocity (m/s)
V = volume (m^3)
x = axial coordinate (m)
Y = total pressure loss coefficient

Greek

γ = isentropic coefficient
η = efficiency
θ = circumferential coordinate
μ = viscosity (kg/m s)
Π = pressure ratio
ρ = density (kg/m^3)
Φ = dissipation function ($1/s^2$)
ω = rotational speed (rad/s)

Subscripts

by = bypass
c,max = compressor
cav = cavity
dr = drum
F = frictional
in = turbine inlet
r = radial coordinate
rel = relative frame
$R1ex$ = rotor1 exit
s = static flow quantity
$S1ex$ = stator1 exit
t = stagnation flow quantity
tt = total-to-total
v = main venturi
x = axial coordinate
θ = circumferential coordinate
1.5 = total-to-static 1.5 stages

Abbreviations

$R1ex$ = rotor1 exit
$S1ex$ = stator1 exit

References

[1] Kobayashi, N., Matsumato, M., and Shizuy, M., 1984, "An Experimental Investigation of a Gas-Turbine Disk Cooling System," ASME J. Eng. Gas Turbines Power, **106**(1), pp. 136–141.
[2] Chew, J. W., Dadkhah, S., and Turner, A. B., 1992, "Rim Sealing of Rotor-Stator Wheelspaces in the Absence of External Flow," ASME J. Turbomach., **114**(2), pp. 433–438.
[3] Dadkhah, S., Turner, A. B., and Chew, J. W., 1992, "Performance of Radial Clearance Rim Seals in Upstream and Downstream Rotor-Stator Wheelspaces," ASME J. Turbomach., **114**(2), pp. 439–445.
[4] Roy, R. P., Xu, G., Feng, J., and Kang, S., 2001, "Pressure Field and Main-Stream Gas Ingestion in a Rotor-Stator Disk Cavity," ASME Paper No. 2001-GT-0564.
[5] McLean, C., Camci, C., and Glezer, B., 2001, "Mainstream Aerodynamic Effects Due to Wheelspace Coolant Injection in a High-Pressure Turbine Stage: Part I—Aerodynamic Measurements in the Stationary Frame'," ASME J. Turbomach., **123**(4), pp. 687–696.
[6] McLean, C., Camci, C., and Glezer, B., 2001, "Mainstream Aerodynamic Effects Due to Wheelspace Coolant Injection in a High-Pressure Turbine Stage: Part II—Aerodynamic Measurements in the Rotational Frame," ASME J. Turbomach., **123**(4), pp. 697–703.
[7] Girgis, S., Vlasic, E., Lavoie, J.-P., and Moustapha, S. H., 2002, "The Effect of Secondary Air Injection on the Performance of a Transonic Turbine Stage," ASME Paper No. GT-2002-30340.
[8] Ong, J. H. P., Miller, R. J., and Uchida, S., 2006, "The Effect of Coolant Injection on the Endwall Flow of a High Pressure Turbine," ASME Paper No. GT2006-91060.
[9] Paniagua, G., Denos, R., and Almeida, S., 2004, "Effect of the Hub Endwall Cavity Flow on the Flow-Field of a Transonic High-Pressure Turbine," ASME J. Turbomach., **126**(4), pp. 578–586.
[10] Boudet, J., Hills, N. J., and Chew, J. W., 2006, "Numerical Simulation of the Flow Interaction Between Turbine Main Annulus and Disc Cavities," ASME Paper No. GT-2006-90307.
[11] Reid, K., Denton, J., Pullan, G., Curtis, E., and Longley, J., 2006, "The Effect of Stator-Rotor Hub Sealing Flow on the Mainstream Aerodynamics of a Turbine," ASME Paper No. GT-2006-90838.
[12] Marini, R., and Girgis, S., 2007, "The Effect of Blade Leading Edge Platform Shape on Upstream Disk Cavity to Mainstream Flow Interaction of a High-Pressure Turbine Stage," ASME Paper No. GT2007-27429.
[13] Sell, M., Schlienger, J., Pfau, A., Treiber, M., and Abhari, R. S., 2001, "The 2-Stage Axial Turbine Test Facility LISA," ASME Paper No. 2001-GT-0492.
[14] Behr, T., Kalfas, A. I., and Abhari, R. S., 2007, "Unsteady Flow Physics and Performance of a One-and-1/2-Stage Unshrouded High Work Turbine," ASME J. Turbomach., **129**(2), pp. 348–359.
[15] Kupferschmied, P., Kopperl, O., Gizzi, W. P., and Gyarmathy, G., 2000, "Time Resolved Flow Measurements With Fast Aerodynamic Probes in Turbomachinery," Meas. Sci. Technol., **11**, pp. 1036–1054.
[16] Pfau, A., Schlienger, J., Kalfas, A. I., and Abhari, R. S., 2003, "Unsteady, 3-Dimensional Flow Measurement Using a Miniature Virtual 4 Sensor Fast Response Aerodynamic Probe (FRAP)," ASME Paper No. GT2003-38128.
[17] Sharma, O. P., Butler, T. L., Joslyn, H. D., and Dring, R. P., 1985, "3-Dimensional Unsteady-Flow in an Axial-Flow Turbine," J. Propul. Power, **1**(1), pp. 29–38.
[18] Porreca, L., Hollenstein, M., Kalfas, A. I., and Abhari, R. S., 2007, "Turbulence Measurements and Analysis in a Multistage Axial Turbine," J. Propul. Power, **23**(1), pp. 227–234.
[19] Schlichting, H., 1951, *Grenzschicht-Theorie*, G. Braun, Karlsruhe, Germany.
[20] Schuepbach, P., Rose, M. G., Abhari, R. S., Germain, T., Raab, I., and Gier, J., 2008, "Improving Efficiency of a High-Work Turbine Using Non-Axisymmetric Endwalls. Part II: Time-Resolved Flow Physics," ASME Paper No. GT2008-50470.